Materials Science & Engineering A 672 (2016) 175–183

Contents lists available at ScienceDirect

Materials Science & Engineering A

journal homepage: www.elsevier.com/locate/msea

Strengthening mechanisms in an Al-Fe-Cr-Ti nano-quasicrystalline alloy and composites

S. Pedrazzini [a,*], M. Galano [a], F. Audebert [a,b,c], D.M. Collins [a], F. Hofmann [d], B. Abbey [e], A.M. Korsunsky [d], M. Lieblich [f], A. Garcia Escorial [f], G.D.W. Smith [a]

[a] Department of Materials, University of Oxford, Parks Road, Oxford OX1 3PH, UK
[b] INTECIN, School of Engineering, University of Buenos Aires, Paseo Colon 850, Ciudad de Buenos Aires, Argentina
[c] Department of Mechanical Engineering and Mathematical Sciences, Oxford Brookes University, Wheatley Campus, OX33 1HX Oxford, UK
[d] Department of Engineering Science, University of Oxford, Parks Road, Oxford OX1 3PJ, UK
[e] ARC Centre of Excellence in Advanced Molecular Imaging, La Trobe University, Victoria 3086, Australia
[f] Department of Physical Metallurgy, CENIM-CSIC, Avda. Gregorio del Amo 8, Madrid, Spain

ARTICLE INFO

Article history:
Received 1 June 2016
Accepted 2 July 2016
Available online 3 July 2016

Keywords:
Aluminium
Quasicrystals
Mechanical properties
Strengthening mechanisms
Fibre composites

ABSTRACT

We report a study of the structure-processing-property relationships in a high strength $Al_{93}Fe_3Cr_2Ti_2$ nano-quasicrystalline alloy and composites containing 10 and 20 vol% ductilising pure Al fibres. The superimposed contributions of several different strengthening mechanisms have been modelled analytically using data obtained from systematic characterisation of the monolithic alloy bar. An observed yield strength of 544 MPa has been substantiated from a combination of solid solution strengthening, work hardening, precipitation hardening and Hall-Petch grain size dependent effects. These materials have been shown by other authors in previous published work to be highly sensitive to the size distribution of particles in the powder from which they are made, and the subsequent thermomechanical processing conditions. The processing condition employed in this study provided micron-sized grains with a strong [111] preferential orientation along the extrusion direction and a bimodal size distribution of the icosahedral nano-quasicrystalline precipitates. Both were deemed to be a significant contributor to the high yield strength observed. The addition of pure Al fibres was found to decrease the yield strength linearly with increasing Al content, and to augment the ductility of the composites.

1. Introduction

Novel, high performance aluminium-based alloys with nano-scale dispersoid phases offer exceptional mechanical properties, far superior to conventional aluminium alloys, making them attractive for widespread use in automotive and aerospace applications. In particular, nano-quasicrystalline Al-based alloys, produced through a rapid solidification process, have shown excellent tensile and specific strength properties [1–3]. However, their use has been limited by temperature sensitivity both during service and thermo-mechanical processing and the variation in performance depending on the bulk processing route used. Galano et al. [4] demonstrated that the addition of Ti, V, Nb or Ta alloying elements improves the thermal stability of the icosahedral phase within Al-Fe-Cr alloys in melt-spun ribbons.

Rapid solidification can be achieved by a number of methods, however gas atomisation is one of the few methods that can be used on an industrial scale. The influence of processing parameters during consolidation and their effect on the mechanical properties of the extruded material have been tested on nano-quasicrystalline $Al_{93}Fe_3Cr_2Ti_2$ at% alloy by Todd et al. [2]. They found that increasing the extrusion ratio of 25–50 μm powders from 10:1 to 14:1 at 400 °C provides a $<3\%$ increase in yield strength. Decreasing the powder particle size from 50 to 100 μm to 25–50 μm caused a much more substantial $\sim 35\%$ increase in yield strength during quasi-static, room temperature tensile tests. It is worth mentioning that Todd et al. [2] found a larger proportion of quasicrystals in the powder sizes between 25 and 50 μm than in the 50–100 μm range.

Systematic studies of nanostructured Al-based melt-spun ribbons to assess the resulting tensile strengths were conducted at room temperature by Audebert et al. [5] and at 350–500 °C by Galano et al. [3]. Each study suggested that the outstanding mechanical properties of the alloys were due to the combined effect of solid solution strengthening, particle dispersion and grain refinement strengthening. The influence of each strengthening mechanism on the resulting behaviour was not quantified in these studies. However, a study was performed on an $Al_{92.4}Fe_{1.2}Cr_{3.3}Ti_{2.4}Si_{0.7}$ at% alloy produced by powder metallurgy

* Corresponding author.

http://dx.doi.org/10.1016/j.msea.2016.07.007

and extruded at 450 °C from powder particles sizes < 45 μm. The authors found that the Hall-Petch effect was the most dominant mechanism [6]. Vojtěch et al. [6] found that the Orowan strengthening effect was the next largest contributor, whilst solid solution strengthening was deemed to be negligible due to the hot processing method used. This assumes that a low solute content is retained in solid solution in the matrix following rapid solidification, heat treatment and thermal-mechanical processing.

Whilst the specific mechanical strength of nano-quasicrystalline $Al_{93}Fe_3Cr_2Ti_2$ at% alloys is far superior to any current commercial Al-based alloys, their ductility and strain to failure have thus far proven inferior. Nagy et al. [7], working with bars made by cryomilling a melt-spun $Al_{94}V_4Fe_2$ (at%) alloy with < 1 μm pure Al powder then extruding at 420–450 °C, improved the overall ductility of the composites in comparison to the monolithic $Al_{94}V_4Fe_2$ alloy. In the present work, the correlation between the microstructure and mechanical properties of bulk processed nano-quasicrystalline $Al_{93}Fe_3Cr_2Ti_2$ at% alloy and composites with 10 and 20 vol% pure Al ductilising fibres has been investigated. A suite of multi-scale characterisation and mechanical testing tools have been used to quantify the contributions of different strengthening mechanisms to the overall strength of the alloy, then the rule of mixtures was used to predict the strength of the composites.

2. Experimental procedure

Gas atomised powder of nominal chemical composition $Al_{93}Fe_3Cr_2Ti_2$ and commercially pure Al powder were provided by Alpoco Ltd. and sieved to < 25 μm. The powders were then weighed, mixed and packed into an Al can without prior compaction or degassing and extruded at CENIM, Madrid. Extrusions were performed at 380–400 °C, with a ram velocity of 0.3 mm/s and an extrusion ratio of 14:1. The conditions were selected based on the study performed by Todd et al. [2]. This process produced three bars ~1 m long and 12 mm in diameter prior to the removal of the extrusion can from each surface.

To visualise fibre distributions in 3D and to assess the content of residual porosity present in the samples, synchrotron X-ray micro-tomography was performed at the TOMCAT beamline at the Swiss Light Source (SLS). Two samples of size 1 mm diameter of each material containing nominally 0, 10 and 20 vol% pure Al fibres

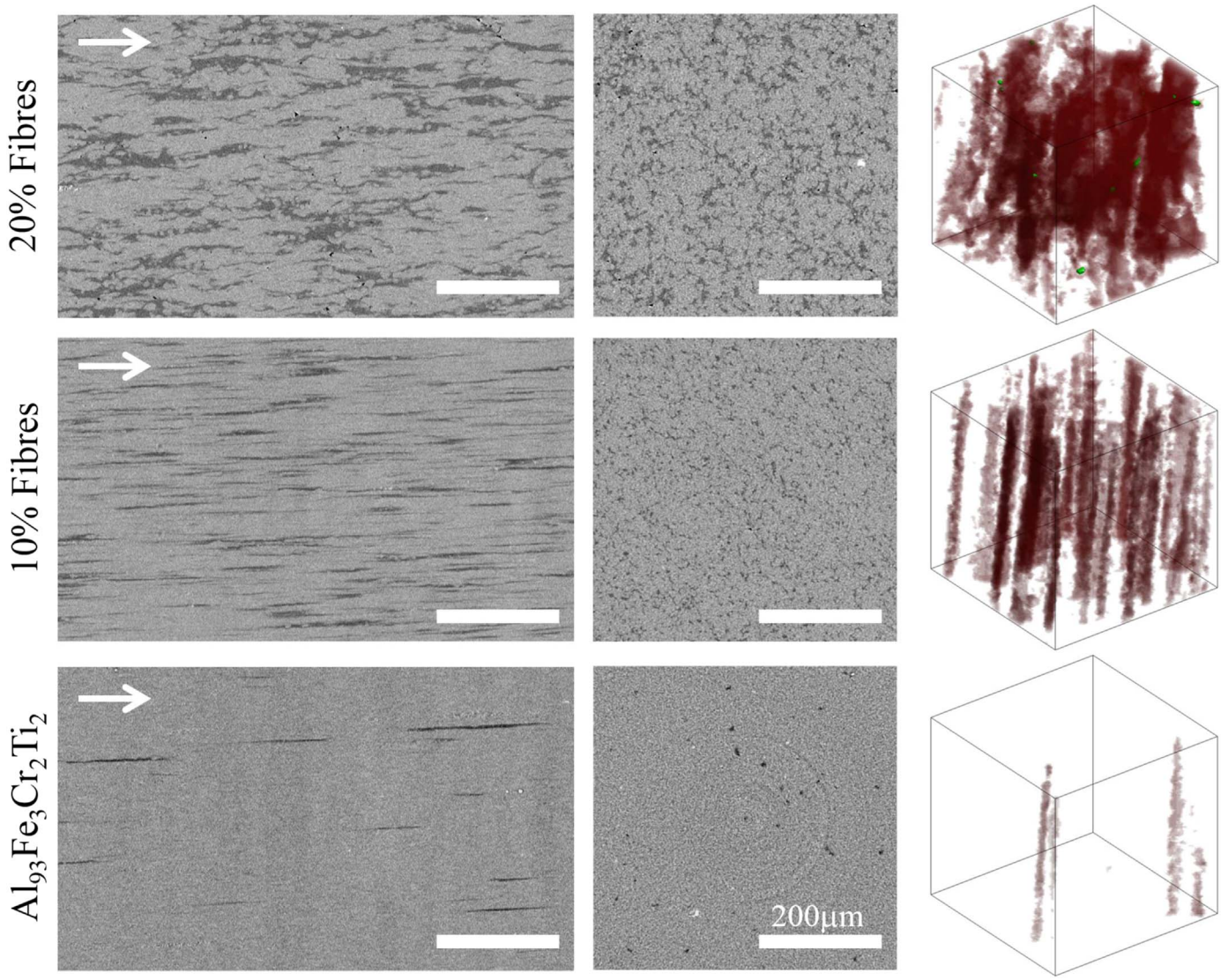

Fig. 1. X-ray tomography micrographs showing the distribution of pure Al fibres (dark grey) within the Al-Fe-Cr-Ti alloy matrix (lighter grey) for samples containing nominally 20%, 10% and 0% fibres. Longitudinal sections parallel (indicated by an arrow) and cross sections perpendicular to the extrusion direction are shown. Also shown are 3D cubes reconstructed and segmented from the tomography data. Fibres are rendered in translucent red, whilst voids (visible in the "20% Fibres" data) are rendered in green. The size of the rendered cubes is $74 \times 74 \times 74$ μm^3.

were examined. The incident beam was monochromatised to a photon energy of 20 keV. Near field radiographs were collected using a 20 μm thick YAG: Ce scintillator coupled to an optical objective lens, resulting in a field of view of 1.5×1.5 mm^2 and a nominal pixel size of 0.74×0.74 μm^2. For each scan 1201 projections were collected over a 360° rotation with an acquisition time of 700 ms per projection. Fig. 1 shows reconstructed micrographs of the imaged samples, sectioned parallel and perpendicular to the extrusion direction. Representative volume rendered reconstructions of the samples show the distribution of fibres (red translucent) and voids (green), whilst the matrix is not displayed.

X-Ray diffraction (XRD) was performed on each bar to identify the phases present, using a Philips 1810 θ–2θ diffractometer with Cu-Kα radiation. Scans covered 2θ angles from 20 to 100° (scattering vector Q between 1.4–4.0 Å^{-1}) with a tube voltage of 35 kV, current of 50 μA and a scanning step size 0.02°.

Electron backscatter diffraction (EBSD) was performed on sections of the monolithic alloy bar in a JEOL 6500F microscope equipped with an EBSD detector and TSL OIM software. A working distance of 15 mm was used, the samples were tilted at 70°, operating at a beam current of 13 nA and a voltage of 15 kV. To provide the best Confidence Index when fitting the diffraction patterns, the camera was used with 1×1 binning and an acquisition time of 0.94 s per pattern. A binned pattern size of 120, a peak symmetry of -0.55 and a rho function of 83% were used. Grain size was determined from the mean and standard deviation of the collected data.

Transmission electron microscopy (TEM) was performed on the monolithic alloy bar, using a Gatan dimple grinder and Gatan Precision Ion Polishing System for sample preparation. Specimens of the alloy powder prior to extrusion were prepared using a Zeiss NVision 40 focused ion beam, by milling and lifting out sections of powder particles. Each specimen was examined using a Philips CM20 W-filament microscope with an Oxford Instruments Energy Dispersive X-ray detector (EDX). Diffraction patterns were obtained, however, very often the particles present in the microstructure were too small to use the smallest selected area aperture. Convergent beam diffraction had to be performed using the smallest spot sizes, which, when converged, allowed diffraction patterns to be taken from microstructural features as small as ~40 nm. From the micrographs acquired, particle size distributions were determined through manual measurements. Automated measurements were deemed unreliable due to higher error margins arising from particle overlap, thickness fringes and diffraction effects being incorporated into the measurements. Samples were tilted to check for particle overlap and ensure accuracy of the measurements.

Particle size distributions and mean size were obtained by fitting the measured particle sizes with a Gaussian function using Origin 8.5.1 software. A minimum of 120 measurements performed on various locations of one 3 mm disc sample were used for the fitting with full width half maximum values used as the associated particle size spread. The matrix compositions of each specimen were measured by TEM-EDX, with the values presented here obtained by taking the mean value from a minimum of 10 measurements.

Vickers microhardness measurements were made on the extruded monolithic alloy bar and composites using a load of 500 g applied for 20 s. Reported results are mean values ± standard deviations calculated for 25 indents measured. Indents were > 150 μm in diameter and are therefore considered representative of the overall microstructure as each would encompass several grains and quasicrystalline particles. Finally, tensile tests were performed at room temperature using an Instron servo-hydraulic mechanical tester by Westmoreland Plc at a strain rate of 1×10^{-4} s^{-1}. The strain was measured by means of an extensometer. The samples size was selected following ASTM E 8/E 8M – 08 standard, using the sub-size specimen 4 specification with a gauge length 16 mm and diameter 4 mm.

3. Results

X-ray tomography micrographs displayed in Fig. 1 show cross sections and longitudinal sections of the $Al_{93}Fe_3Cr_2Ti_2$ alloy sample and the composites with 10 and 20 vol% fibres. The extrusion process fully consolidated the monolithic alloy bar leaving no evidence of residual porosity. Some pure Al contamination – about 0.35 vol% – was detected, originating from the standard industrial practice of cleaning the atomiser with pure Al between runs of different alloys. The contamination appears to be randomly distributed throughout the sample, and is particularly evident in the 3D rendering. In both composite samples, a distribution of short pure Al fibres is visible, aligned along the extrusion direction in the longitudinal section, < 200 μm in length and < 50 μm in diameter. Both the cross section and 3D rendering volumes show that the Al fibre distribution is uniform within the matrix indicating that the original powders were well mixed before extrusion and no clustering of the Al fibres occurred. The difference in strength between the pure Al and quasicrystalline Al-Fe-Cr-Ti alloy powders noticeably affects the shape of the fibres. In the pure alloy bar and the bar with 10 vol% pure Al fibres large amounts of plastic deformation from the extrusion procedure, results in the fibres adopting more linear, elongated shapes. As the strength of the composite decreases with the addition of 20 vol% pure Al, the plastic deformation experienced by the fibres is reduced, allowing them to maintain a more convoluted morphology. A porosity of 2×10^{-4} vol% was observed only in the composite sample containing 20 vol% fibres.

The phases present in each material have been identified using X-ray diffraction, as shown in Fig. 2. The reflections present for the pure Al powder are identified as α, with evidence of this phase present in the Al alloy powder, bar, and samples with the Al fibre additions. For samples containing Al-Fe-Cr-Ti, the icosahedral quasicrystalline phase is present, with reflections strongest for the Al-Fe-Cr-Ti powder sample. The reflections of the icosahedral phase have been indexed following the work of other authors [4]. An additional peak at 2.4 Å^{-1} present in the diffractogram of the Al-Fe-Cr-Ti alloy powder was assigned to the metastable θ-Al_{13}(Cr, Fe)$_{2–4}$. This phase has been reported to have a distorted monoclinic crystal structure produced by rapid solidification [8–11], and therefore expected following the gas atomisation procedure used for the production of this sample. Due to overlaps only one reflection is observed, therefore unambiguous determination of this phase is difficult. However, its presence is expected in small volume fractions with its strongest peak ($\bar{8}20$) overlapping with the FCC-Al (200) peak, the second strongest reflections the ($\bar{4}24$) and (331) overlapping with two icosahedral peaks. The ($\bar{1}31$) reflection in the position observed here, so the highest intensity peak which does not overlap with other reflections. Following extrusion at 380–400 °C, the reflection at 2.4 Å^{-1} from the θ-Al_{13}(Fe, Cr)$_{2–4}$ phase can no longer be distinguished, indicating this phase is no longer present. The warm extrusion process did not cause the decomposition of the icosahedral phase, which is consistent with previous studies in which an extrusion temperature of 400 °C was used [2].

Microstructural analysis by TEM was utilised to confirm the phases observed by XRD and observe their distribution within the FCC-Al matrix. Fig. 3(a) and (b) show bright field TEM micrographs and the five-fold symmetry convergent beam diffraction pattern of the icosahedral phase presents in Al-Fe-Cr-Ti alloy atomised powder and (c) and (d) show the same for the extruded bar. Both

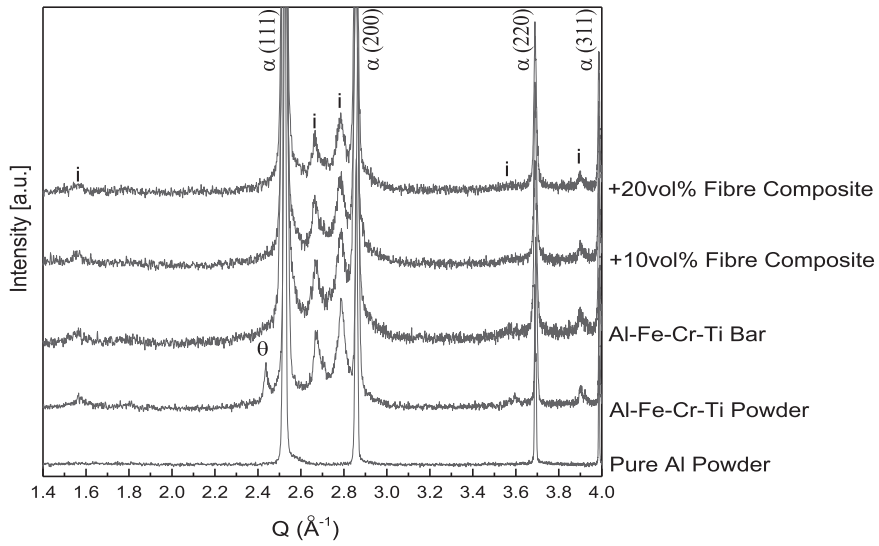

Fig. 2. X-ray diffractogram of the pure $<25\,\mu m$ Al-Fe-Cr-Ti alloy and pure Al powders and a longitudinal section of the warm extruded bars of Al-Fe-Cr-Ti alloy and composites with 10 vol% pure Al fibres and with 20 vol% pure Al fibres, showing α-Al and the i-icosahedral phase. The reflection at 2.4 Å^{-1} was assigned to the metastable θ-$Al_{13}(Fe\text{-}Cr)_{2\text{–}4}$ phase.

the as-atomised powder and the extruded bar contain icosahedral quasicrystalline particles embedded in the α-Al matrix. Qualitatively, no noticeable size difference after warm extrusion was observed for the icosahedral particles, however, no attempts were made to measure accurate particle size distributions in the as-atomised powder. The measured chemical composition of the α-Al matrix by TEM-EDX before and after extrusion was shown to be similar (Table 1). In each case, a higher solute content than the equilibrium solid solubility of Fe, Cr and Ti in Al was found even after thermal – mechanical forming through extrusion between 380 and 400 °C [12,13].

Several authors have performed independent characterisation of extruded bars and melt-spun ribbons of alloys similar to the one used in this study and have reported the presence of icosahedral phase dispersoids in the α-Al matrix, though with small fractions, varying size and compositions of other intermetallics phases present. These include evidence of $Al_{13}Fe_4$ and $Al_{13}Cr_2$ [8], metastable θ-$Al_{13}(Fe, Cr)_{2\text{–}4}$ [8–11], Al_6Fe [14,15], $Al_{23}Ti_9$ [1,2], or Al_3Ti [14,15]. In the combined XRD and TEM results, with the exception of the θ-phase in the X-ray diffractogram of the alloy powder, none of these or any other intermetallics were observed.

Icosahedral particle size distributions were measured in the extruded bars, with over 120 diameter measurements taken and plotted against the relative frequency in Fig. 4. Following the method outlined by Ashby [16], stereology structure factors were calculated assuming all particles were spherical and that measurements were obtained from planar surfaces. The particle sizes were calculated by using:

$$r_v = \sqrt{\frac{3}{2}} r_s \tag{1}$$

where r_s is the mean radius of intersection with a 2D planar surface, r_v is the 3D particle radius. The number of particles intersecting a unit area N_s was then measured and used to calculate the volume fraction, f, using

$$f = N_s \frac{2}{3} \pi r_v^2 \tag{2}$$

The mean planar centre-to-centre particle separation $2R_s$ (also referred to as λ) was calculated using the necessary approximation of assuming particles are arranged at locations equivalent to atoms on an FCC lattice [16].

$$2R_s = \sqrt{\frac{4}{f}} \sqrt{\frac{2}{3}} r_v \tag{3}$$

The icosahedral particle size distribution was found to be bi-modal, with mean particle radii $r_1 = 43 \pm 6$ nm and $r_2 = 129 \pm 6$ nm. Using the equations described above, volume fraction and the inter-particle spacing was calculated for both the larger and smaller particle radii. For r_1, the partial volume fraction was $f_1 = 0.15$ and $2\,R_{s1} = 1.8 \times 10^{-7}$ m. For r_2, the partial volume fraction was calculated to be $f_2 = 0.26$ and $2R_{s2} = 4.12 \times 10^{-7}$ m. The overall volume fraction, assuming the contributions from each distribution of quasicrystalline and intermetallic particles could be added linearly, was calculated as $f = 0.41$. This result appears consistent with previously reported values of $f = 0.42$ [5] in melt-spun ribbons of the same composition, and the value from Inoue et al. [17] who measured $f = 0.45$.

EBSD measurements showed evidence of "bands" of equiaxed grains and sub-grains separated by low angle ($<15°$) boundaries along the extrusion direction (Fig. 5a). As an approximation, the area of each grain was measured and equivalent diameter values were calculated assuming each grain can be approximated as a sphere. These measurements represent planar surface diameters. The geometric method used to extrapolate 3D grain sizes from 2D surface measurements, as given by Eqs. (1)–(3), was originally developed by Ashby [16] to describe the structure factors of particles in a matrix. The geometric similarity between grains and precipitates enables each of their diameters and volume fractions to be treated in the same manner [18]. Fig. 5(a) shows the data collected represented as an inverse pole figure map. However for grain size calculations, any apparent "grains" smaller than 400 nm were assumed to be noise in the EBSD maps as that is the smallest grain size and/or subgrain size that could be observed from the TEM sample analysed. Using these parameters, the mean and standard deviation were calculated to be $d_s = 0.97 \pm 0.3\,\mu m$. Fig. 5 (b) shows the inverse pole figure obtained from the EBSD scan, which indicates that after extrusion the sample has a preferred grain orientation (texture) along the [111] direction.

Vickers microhardness was measured along the extrusion direction of the monolithic alloy, obtaining a value of $\mu HV_{500} = 207 \pm 2$. The composites with 10 and 20 vol% fibres were

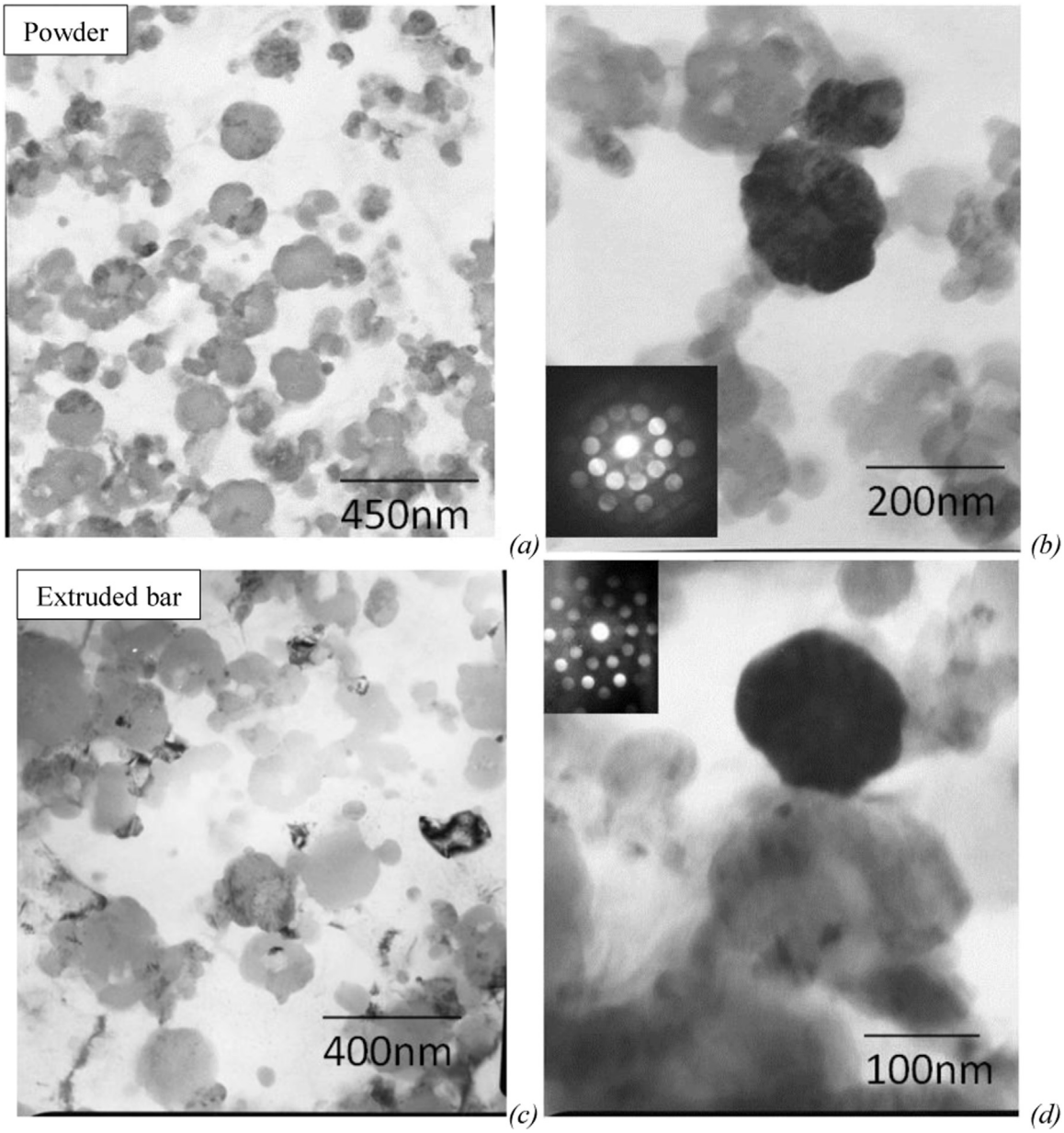

Fig. 3. Bright field TEM micrographs of a single as-atomised powder particle illustrating (a) the overall microstructure and (b) icosahedral phase with its characteristic convergent beam diffraction pattern from a five-fold axis orientation. Bright field TEM micrographs of the consolidated bar after extrusion at 400 °C showing (c) the overall microstructure and (d) icosahedral phase with its corresponding five-fold convergent beam diffraction pattern.

Table 1
solid solubility of Fe, Cr and Ti in Al at 400 °C taken from the literature [12,13] compared to the composition of the bars and the powder.

	Maximum Extrusion Temp	Matrix composition at%			
		Al	Fe	Cr	Ti
Equillibruim Solid Solubility in Al at 400 °C	At 400 °C	–	0.02	0.18	0.032
Powder	n/a	98.2	0.2	0.3	1.4
Al-Fe-Cr-Ti	400	98.2	0.2	0.4	1.3
+10 vol% Al	388	98.2	0.4	0.2	1.3
+20 vol% Al	389	98.1	0.2	0.4	1.3

measured to be $\mu HV_{500} = 173 \pm 6$ and 140 ± 9 respectively. Other authors measured the micro hardness of the same monolithic alloy: Todd et al. [2] found for a $Al_{93}Fe_3Cr_2Ti_2$ alloy extruded from the same powder size and extrusion temperature, though with an extrusion ratio of 10:1 instead of 14:1, the microhardness was $\mu HV_{25} = 172 \pm 9$. Galano et al. [3] observed a high microhardness of $\mu HV_{100} = 351$ for melt-spun ribbons of the same nominal chemical composition. These hardness values are significantly higher than those of commercial high strength Al-based alloys, such as HV = 172 for 7075 T6, and HV = 155 for 2024 T86 [19].

Tensile engineering stress-strain curves are shown in Fig. 6a, where data were acquired at a strain rate of $1 \times 10^{-4}\,s^{-1}$ on dog-bone shaped threaded specimens. The results of the quasi-static tensile tests gave 0.2% proof stress average values of 544 MPa for the monolithic pure alloy bar and 481 and 411 MPa for the composites containing 10 and 20 vol% pure Al fibres. The strain to failure was also found to increase from 0.064 in the pure alloy bar to 0.074 for both the composites with 10 and 20 vol% pure Al fibres. Young's moduli were measured at 69 GPa for the pure alloy and 66 GPa (10% fibres) and 56 GPa (20% fibres). Each test was

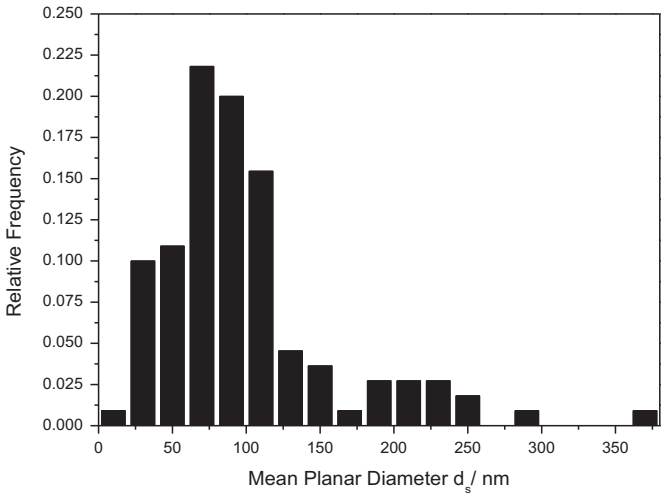

Fig. 4. Plot of the icosahedral particles sizes and their relative frequency measured from TEM micrographs of the extruded Al-Fe-Cr-Ti alloy bar. 120 measurements were taken and plotted.

repeated twice and the stress and strain error range (scatter) was found to be $<0.02\%$. Both the yield strength and UTS of the composites were found to decrease linearly with increasing volume fraction of pure Al fibres, as shown in Fig. 6b.

4. Discussion

The active strengthening mechanisms which contribute to the yield strength of the material can be assigned to microstructural features, such as solutes in solid solution, dislocation (sub-) structures, grain size, particle/dispersoid size and distribution, texture, etc. Superposition of various strengthening mechanisms has remained an unsolved problem and various additivity laws, e.g. linear superposition, quadratic superposition or more complex relations, have been proposed so far [20]. However, linear superposition remains the most common choice [6], therefore in the present work a linear additivity law was adopted for the different strengthening mechanisms analysed.

Previous studies on melt spun nano-quasicrystalline Al-Fe-Cr-Ti alloy showed that the main contributors to the high yield strength were the small grain size [3,5,6], the presence of nanoparticles

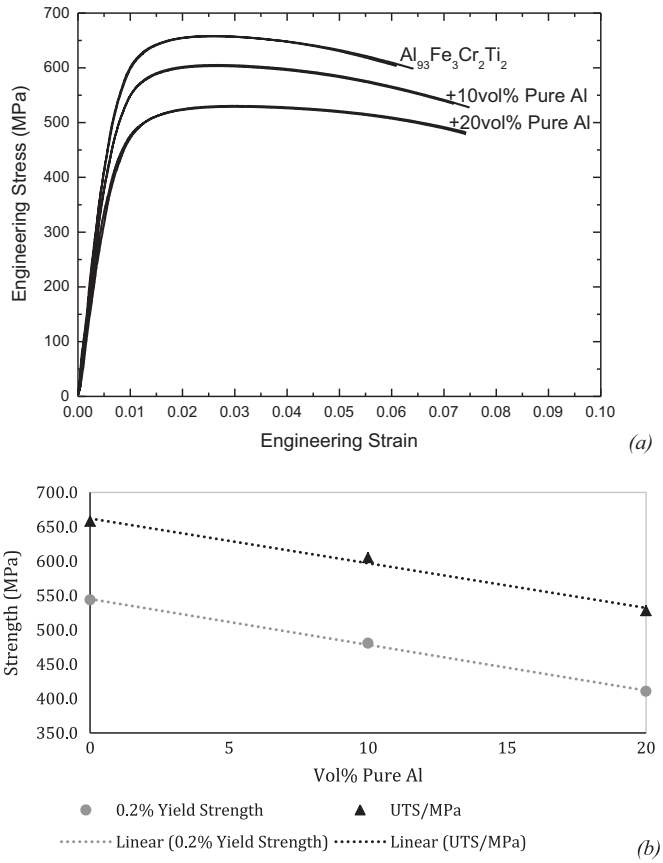

Fig. 6. (a) Quasi-static tensile engineering stress-strain curves obtained from the pure Al-Fe-Cr-Ti bar and the composites with 10 and 20 vol% pure Al fibres performed at room temperature and $1\times10^{-4}\,s^{-1}$ strain rate, (b) plot of UTS versus vol% pure aluminium fibres showing a linear decrease in strength as pure Al fibre content is increased.

(quasicrystals and intermetallics) [3,5,6] and the supersaturation of elements in solid solution [3,5]. Vojtěch et al. [6] suggested the solid solution strengthening mechanism could be negligible for an $Al_{92.4}Fe_{1.2}Cr_{3.3}Ti_{2.4}Si_{0.7}$ at% alloy extruded at 450 °C. They found Hall-Petch and Orowan mechanisms to be the main contributors to the overall yield strength in that case.

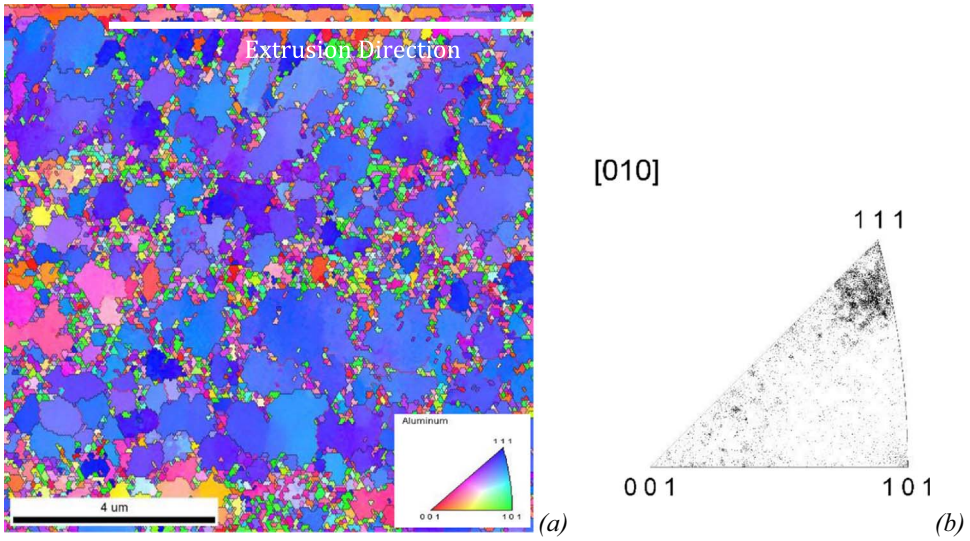

Fig. 5. (a) EBSD map showing the grains within the nano-quasicrystalline alloy along the extrusion direction (horizontal, as indicated by the arrow) and pole figure showing the grain orientations in the map (b) inverse pole figure showing the grain orientations and texture trends along the extrusion direction.

4.1. Particle strengthening

Precipitates hinder dislocation mobility by forcing them to shear weak obstacles or bypass stronger ones (Orowan strengthening). In either case the stress required for a dislocation to propagate on its slip plane is increased, therefore augmenting the yield strength of the material. Icosahedral particle shearing has never been observed in the published scientific literature [5,8]. Thus, Orowan strengthening is expected to be the main active particle strengthening mechanism in the present alloy. Eq. (4) is used to calculate the stress required for dislocations to bypass impenetrable obstacles according to Orowan's model.

$$\sigma_p = \frac{MGb}{2R_s} \tag{4}$$

where G is the bulk shear modulus of the matrix (for Al, G = 26.2 GPa [6,19]), b is the Burgers vector (for Al, b = 0.286 nm [6]), $2R_s$ is the inter-particle spacing [6,19,21], and M is the Taylor factor, which for most materials can be assumed to be ~3 [6]. However, in a FCC material for a [100]-oriented grain deformed in tension M[100]=2.45 while it is 50% higher for the [111]-orientation with M[111]=3.67. Considering the substantial texture observed in the [111] direction in the EBSD shown in Fig. 5 for the $Al_{93}Fe_3Cr_2Ti_2$ alloy, in the present work we adopted a Taylor factor of M = 3.5.

In the present study, the observed particle size distribution was bimodal. The presence of small fractions of larger quasicrystalline particles in comparison with the average particle size (creating bimodal distributions in the alloy) was also observed by other authors in melt-spun nano-quasicrystalline alloys [10,22]. Using the mean particle size radii obtained from TEM, r_1 and r_2, along with the corresponding $2R_s$ and f values for each, the Orowan equation was employed, adding the two contributions linearly according to their relative fractions. This yields $\Delta\sigma_P \approx 210$ MPa.

Assumptions made in order to perform these calculations are that particles are evenly spaced, spherical in shape and act as impenetrable obstacles to dislocations. Further refinements to Orowan's model have been performed by Foreman and Makin [23] to account for the effect of non-regular distributions of obstacles using the concept of effective obstacle spacing. Later, Hirsch and Humphreys [24] and Bacon [25] proposed elastic field screening models, which impose a logarithmic dependency of dislocation line energy and capture the effect of precipitate finite size. Alternatively, Dislocation Dynamics (DD) simulations could be used to monitor plastic deformation, where significant recent advances are enabling microstructures close to reality to be modelled [26–28]. In these examples of modified or more complex strengthening models, Orowan's mechanism is typically considered as solely responsible for the overall strength, rather than a superposition of strengthening mechanisms as is present for material examined in this study. Multi-component models accounting for such complex behaviour are presently not available and hence this work relies on microstructural simplification to approximate the yield strength.

Several studies that compare the contributions of Orowan and Hall-Petch strengthening mechanisms to the macroscopic material response have been reported. Ehrstrom et al. [21] found that the Hall-Petch effect is most dominant in rapidly solidified Al-Fe-X alloys (where X is Zr, Mo, Si, etc.), whilst Vojtěch et al. [6] replicated this conclusion in an Al-Fe-Cr-Ti-Si alloy. Furthermore, a study of rapidly solidified Al-Cr-Zr suggested that the Orowan effect was negligible compared to the Hall-Petch effect [29]. Therefore, even on very similar alloy systems, the strengthening mechanisms appear exceptionally sensitive to subtle variations in the processing methods and their resulting microstructures. Assuming the Orowan effect is the dominant strengthening mechanism in this study, and only accounting for the incoherent particles, would clearly be wrong, as the calculated $\Delta\sigma_p$ value is far less than the experimentally measured yield strength value of 544 MPa.

4.2. Grain boundary strengthening

The Hall–Petch relation [30] (Eq. (5)) was shown to be an accurate analytical expression for yield strength predictions in polycrystalline alloys. Originally, Hall and Petch utilised the theoretical model of an equilibrated pile-up of edge dislocations at the grain boundary developed by Eshelby et al. [31]. They predicted that the development of intra-granular dislocation pile-ups would have a slip length proportional to the inverse square root of the mean grain size, which they validated with empirical measurements. Improvement of the pile-up model was given later by [32]. Other authors have also derived the Hall–Petch behaviour by measuring dislocation density within grains through TEM observations and by determining the increase of the plastic flow stress with the square root of dislocation density [33,34]. Grain boundaries were also found to be common sources of dislocations [35,36]. Either way, the pile-up hypothesis with a classical -0.5 exponent is widely used to explain the Hall–Petch behaviour of the yield stress [37].

The yield stress calculated from the empirically derived Hall-Petch effect is given by Eq. (5), [30].

$$\sigma_{gb} = \sigma_0 + \frac{k}{\sqrt{d}} \tag{5}$$

where σ_o is the lattice frictional stress, k is the Hall-Petch coefficient which is strongly influenced by the microstructural state of the alloy and d is the average grain size. For pure Al, σ_o is commonly taken as ~16 MPa [19,38]. The constant, k, is known as the "locking parameter", which measures the relative hardening contribution of the grain boundaries [37]. In this study it was deemed appropriate to use empirical values measured on high solute concentration Al alloys with fine grain sizes, k = 0.17 MPa $m^{-1/2}$ [6,29,39]. Assuming the dislocations pile-ups are similar for all the grains in the alloy, k can be considered to be same for all the grains.

In the present work, grain size stereology structure factors were calculated using the method developed by Ashby et al. [16] assuming all grains are spherical and working from measurements from planar surfaces. The 3D grain diameter is therefore $d_v = 1.2 \pm 0.3$ μm. Finally, applying Eq. (5), the grain boundary contribution to the yield stress of the alloy can be estimated as $\sigma_{gb} \approx 141 \pm 17$ MPa.

Recently, Dunstan and Bushby [40] developed an alternative equation to the well-established Hall-Petch relation and fitted it to the tensile stress-strain curves used from Conrad [33], Eshelby [31] and Li [35] as well as many other data-sets providing a fit, which was shown to be more accurate through Bayesian statistical analysis [40]. According to their theory, the relationship between the yield strength and the grain size should be an inverse linear relationship instead of an inverse square root: $\sigma_Y \propto kD^{-1}$ [40]. Either way, for the present work, when their equation is applied instead of the Hall-Petch equation the overall strength prediction remains within the error range quoted.

4.3. Solid solution strengthening

Strength from solid solution hardening arises from strain fields around each solute atom, dependent on the misfit radii of the solute atom. However, quantitative measurements of atomic radii are generally difficult due to the radius not being well-defined,

where its magnitude is affected by electronegativity interactions with the surrounding atoms [41]. A quantitative value of the atomic radii data of atoms in the elemental state obtained through X-ray diffraction was used for the present calculations [19]. Using these values, the lattice misfit caused by atoms in solid solution can be calculated. Friedel's equation for the prediction of the yield strength based on the lattice misfit is [42].

$$\Delta\sigma_y = \alpha f G \Omega_M \frac{\delta}{b} \tag{6}$$

where $\Delta\sigma_y$ is the yield strength increase, $\Omega_M = 1.9 \times 10^{-10}$ for Al 5000 serie alloys, δ is the lattice misfit and b is the burgers vector (=0.286 nm for Al [6]). Using these values, the total contribution to the yield strength from each element of Cr, Ti and Fe in solid solution can be estimated to be as low as ~10 MPa. The solid solution mechanism was also found to be negligible by other authors on rapidly solidified Al-TM alloy systems prepared both by extrusion of atomised powders and extrusion of melt spun, ground ribbons [6,28,43].

4.4. Dislocation-dislocation interactions

The work hardening contribution to the yield strength due to the plastic deformation induced during extrusion must also play an important role in the strength of the $Al_{93}Fe_3Cr_2Ti_2$ alloy. Work hardening as a result of interactions of dislocations with other dislocations and with other barriers to their motion within the lattice can be estimated using the basic equation relating flow stress to structure, with [37]:

$$\Delta\sigma_y \approx M\beta G b\sqrt{\rho} \tag{7}$$

where $\Delta\sigma_y$ is the yield strength increase, β is a constant which is approximately 0.25 for most cases, but can be 0.5–1 depending on the sample crystallography, M is the Taylor factor, G is the bulk shear modulus of the matrix (26 GPa for Al [6]), b is the magnitude of the Burgers vector (0.286 nm in Al at room temperature [6]) and ρ is the density of dislocations. This model provides a work hardening contribution of 183 MPa to the yield strength, with a required dislocation density of $\sim 8 \times 10^{14}\ m^{-2}$. According to the literature, a reasonable value of dislocation density of aluminium samples after a few per cent deformation through cold working should be 10^{12}–$10^{13}\ m^{-2}$. In a heavily cold worked sample this density may be as high as $\sim 10^{15}$–$10^{16}\ m^{-2}$ [44,45]. The extrusion ratio of material tested in this study was 14:1, therefore the dislocation density is expected to be in the higher range. However, this may be an over-estimate due to the high extrusion temperature of 400 °C. At present, there are no values of dislocation density of Al-based samples after warm extrusion around 400 °C available in the literature.

4.5. Mechanical properties of the composites

The UTS and yield strength of the composites decrease linearly with increasing vol% pure Al following the rule of mixtures, as shown in Fig. 6b [46]. The original purpose of the fibre addition was to increase ductility, albeit sacrificing some of the tensile strength to tailor the exact properties to the requirements in specific applications. Both samples with 10 and 20 vol% pure Al fibres have shown a 13.5% increase in ductility. The tests were repeated twice, showing that adding more than 10 vol% pure Al fibres does not further improve ductility. One of the reasons may be the increase in porosity within the 20 vol% pure Al sample.

5. Summary

In summary, the observed microstructure of a $Al_{93}Fe_3Cr_2Ti_2$ nano-quasicrystalline alloy has been correlated to the mechanical strength measured under quasi-static deformation at room temperature. Considering separate mechanisms in turn, several strengthening mechanisms were proposed to be simultaneously active. Contributions from the hard, incoherent particles and grain sizes have been estimated, though these measurements are reliant on an idealised microstructure assumption. This includes perfectly spherical, equally spaced particles and spherical, equiaxed grains separated by high angle grain boundaries. The maximum contribution (~210 MPa) to the yield strength of the extruded $Al_{93}Fe_3Cr_2Ti_2$ alloy bar comes from the Orowan mechanism, arising from the icosahedral particles embedded in the Al matrix. This is to be expected since they constitute 0.41 vol fraction of the material. The second contribution, 141 MPa, appears to come from the small grain size. These contributions alone underestimate the strength of the material, which was 544 MPa, suggesting that additional mechanisms must also contribute. Solid solution hardening is expected to play a minor role, yielding a strengthening effect of ~10 MPa. The remainder of the strength is expected to be a result of dislocation-dislocation interactions (~183 MPa), which are a consequence of the extrusion pressure which yielded a heavily deformed material.

The models used in this study neglected any contributions to the strength from low-angle grain boundaries, giving rise to an additional source of error. The role of porosity, if any, will be the subject of further investigations. It is proposed that the high yield strength of such complex materials may only be fully understood with the use of advanced modelling strategies that can account for coupled strengthening mechanisms. Nevertheless, as no such computational capability currently exists, the relatively straight forward approach adopted here is instructive and clearly identifies the main factors contributing to the overall strength of the alloy and composites.

6. Conclusions

1. An extruded bar produced from atomised powder (< 25 μm) of the $Al_{93}Fe_3Cr_2Ti_2$ at% alloy has been investigated. The extruded material has an exceptionally high tensile strength of 544 MPa at room temperature.
2. Microstructural characterisation revealed that the material comprises an Al matrix with a dispersion of nano-quasicrystalline icosahedral particles. The particles were found to exhibit a bimodal size distribution.
3. Using classical expressions to estimate yield strength contributions, the contribution of hard, incoherent particles, dislocation density, grain boundary and solid solution hardening, yield ~210 MPa, ~141 MPa, ~183 MPa and ~10 MPa respectively. These were each calculated from observations of the microstructure and parameters. It is proposed that these mechanisms are likely to be active simultaneously, explaining the high yield stress.
4. The alloy was also studied as a composite, with the addition of pure Al fibres. Fibres were observed by X-ray tomography to be deformed, and their morphology being an indicator of good bonding with the matrix. Residual porosity was only observed after the addition of 20 vol% fibres while the other bars were fully compacted. Following the rule of mixtures, the yield strength was found to decrease with the addition of pure Al fibres. Ductility was observed to increase with the addition of these fibres at the expense of tensile strength.
5. This report and the creation of the composites with higher ductility opens a promising route forwards towards the production of high strength, lightweight materials whose properties can be tailored individually for specific engineering applications.

Acknowledgements

Industrial collaborator ALPOCO Ltd. (and more specifically Steve McArthur) provided the powders. Dr. Karen Kruska and Dr. Alan Xu assisted with sample preparation of FIB lift-out specimens of the atomised powder for TEM analysis. EPSRC Project EP/E040608/1 provided financial support. M. Galano thanks the RAEng for their support by means of a Research Fellowship. F. Audebert and M. Galano thank PICT-Oxford 2010/2831. F. Audebert also thanks UBACyT 20020130100663 and FONARSEC FS Nano 2010/11 for financial support. Paul-Scherrer Institut, Villigen is acknowledged for the provision of beamtime on TOMCAT beamline at the Swiss Light Source.

References

[1] A. Inoue, H. Kimura, High-strength aluminium alloys containing nanoquasicrystalline particles, Mater. Sci. Eng. A286 (2000) 1–10.
[2] I. Todd, Z. Chlup, J.G. O'Dwyer, M. Lieblich, A. Garcia-Escorial, The influence of processing variables on the structure and mechanical properties of nanoquasicrystalline reinforced aluminium alloys, Mater. Sci. Eng. A 375–377 (2004) 1235–1238.
[3] M. Galano, F. Audebert, I.C. Stone, B. Cantor, Nanoquasicrystalline Al-Fe-Cr-based alloys Part II: mechanical properties, Acta Mater. 57 (2009) 5120–5130.
[4] M. Galano, F. Audebert, B. Cantor, I. Stone, Structural characterisation and stability of new nanoquasicrystalline Al-based alloys, Mater. Sci. Eng. A 375–377 (2004) 1206–1211.
[5] F. Audebert, F. Prima, M. Galano, M. Tomut, P.J. Warren, I.C. Stone, B. Cantor, Structural characterisation and mechanical properties of nanocomposite Al-based alloys, Mater. Trans. A 43 (8) (2002) 2017.
[6] D. Vojtěch, J. Verner, J. Šerák, F. Simancik, M. Balog, J. Nagy, Properties of thermally stable PM Al-Cr based alloy, Mater. Sci. Eng. A 458 (1–2) (2007) 371.
[7] J. Nagy, M. Balog, K. Ibdinskc, F. Simandek, P. Švec, D. Janidkovid, High strength potential of aluminium nanocomposites reinforced with nonperiodical phases, Int. J. Mater. Prod. Technol. 23 (1–2) (2005) 79–90.
[8] M. Galano, F. Audebert, I.C. Stone, B. Cantor, Nanoquasicrystalline Al-Fe-Cr-based alloys: Part I: phase transformations, Acta Mater. 57 (2009) 5107–5119.
[9] J. Copola, F. Audebert, S. Duhalde, Quasicrystalline Al-based alloys by physical Laser deposition, J. Met. Nanocryst. Mater. 14 (2002) 14, 27.
[10] F. Audebert, R. Colaco, R. Vilar, H. Sirkin, Laser cladding of Al-based quasicrystalline alloys, Scr. Mater. 40 (1999) 551.
[11] R. Manaila, V. Florescu, A. Jianu, O. Radulescu, On the transition-metal quasisublattice in icosahedral Al-Cr-Fe phases, Philos. Mag. B 60 (1989) 589.
[12] T.B. Massalski, H. Okamoto, P.R. Subramian, L. Kacrzak (Eds.), Binary Alloy Phase Diagrams, Materials Park (OH): ASM International, 1990.
[13] L. Xu, Y.Y. Cui, Y.L. Hao, R. Yang, Mater. Sci. Eng. A 435–436 (2006) 638–647.
[14] A. Garcia-Escorial, M. Echevarria, M. Lieblich, I. Stone, Characterisation of an Al93Fe3Cr2Ti2 alloy obtained by spray forming, J. Alloys Comp. 504S (2010) S519–S521.
[15] M. Yamasaki, Y. Nagaishi, Y. Kawamura, Inhibition of Al grain coarsening by quasicrystalline icosahedral phase in the rapidly solidified powder metallurgy Al-Fe-Cr-Ti alloy, Scr. Mater. 56 (9) (2007) 785–788.
[16] M. Ashby, The hardening of metals by non-deforming particles, Z. Met. 55 (1964) 5–17.
[17] A. Inoue, H. Kimura, High elevated-temperature strength of Al-based nanoquasicrystalline alloys, Nanostruct. Mater. 11 (1999) 221–231.
[18] E.E. Underwood, Quantitative Stereology, Addison Wesley 1970, p. 80.
[19] E.A. Brandes, G.B. Brooks (Eds.), Smithells Metals Reference Book, 4.21, Butterworth-Heinemann, 1983, pp. 4–25.
[20] A. de Vaucorbeil, W.J. Poole, C.W. Sinclair, The superposition of strengthening contributions in engineering alloys, Mater. Sci. Eng. A 582 (2013) 147–154.
[21] J.C. Ehrstrom, A. Pineau, Mechanical properties and microstructure of Al-Fe-X alloys, Mater. Sci. Eng. A 186 (1994) 55–64.
[22] E.S. Humphreys, P.J. Warren, J.M. Titchmarsh, A. Cerezo, Microstructure and chemistry of Al-V-Fe-Si nanoquasicrystalline alloys, Mater. Sci. Eng. A 304–306 (2001) 844–848.
[23] A.J.E. Foreman, M.J. Makin, Dislocation movement through random arrays of obstacles, Can. J. Phys. 45 (1967) 511.
[24] P.B. Hirsch, F.J. Humphreys, in: A.S. Argon, (Ed.). The physics of strength and plasticity, Cambridge (MA), MIT Press, 1969.
[25] D.J. Bacon, U.F. Kocks, R.O. Scattergood, The effect of dislocation self-interaction on the Orowan stress, Philos Mag. 28 (1973) 1241.
[26] V. Mohles, From forest hardening to strain hardening in body centred cubic single crystals: simulation and modelling, Mater. Sci. Eng. A 309–310 (2001) 265.
[27] V. Mohles, The critical resolved shear stress of single crystal with long-range ordered precipitated calculated by dislocation dynamics simulations, Mater. Sci. Eng. A 365 (2004) 144.
[28] C.S. Shin, M.C. Fivel, M. Verdier, C. Robertson, Dislocation dynamics simulations of fatigue precipitation hardened alloys, Mater. Sci. Eng. A 400–401 (2005) 166.
[29] A. Brahmi, T. Gerique, M. Torralba, M. Lieblich, Flow stress of rapidly solidified Al-5Cr-2Zr alloy as a function of processing variables, Scr. Mater. 37 (1997) 1623–1629.
[30] E.O. Hall, The deformation and ageing of mild steel: III. Discussion of results, Proc. Phys. Soc. Lond. Sect. B 64 (1951) 747.
[31] J.D. Eshelby, F.C. Frank, F.R.N. Nabarro, The equilibrium of linear arrays of dislocations, Philos. Mag. 42 (1951) 351–364.
[32] A.H. Cottrell, Brittle fracture in steels and other metals, Trans. AIME 212 (1958) 192.
[33] H. Conrad, Effect of grain size on the lower yield and flow stress of iron and steel, Acta Metall. 11 (1963) 75–77.
[34] A.W. Thompson, M.I. Baskes, W.F. Flanagan, The dependence of polycrystal work hardening on grain size, Acta Metall. 21 (7) (1973) 1017–1028.
[35] J.C.M. Li, Petch relation and grain boundary sources, Trans. AIME 227 (1963) 239.
[36] H.-H. Fu, D.J. Benson, M.A. Meyers, Analytical and Computational description of effect of grain size on yield stress of materials, Acta Mater. 49 (2001) 2567–2582.
[37] G.E. Dieter, Mechanical Metallurgy, 2nd ed., Mcgraw-Hill, 1988.
[38] E. Hornbogen, E.A. Starke Jr., Theory assisted design of high strength low alloy aluminum, Acta Metall. Mater. 41 (1993) 1–16.
[39] K.L. Kendig, D.B. Miracle, Strengthening mechanisms of an Al-Mg-Sc-Zr alloy, Acta Mater. 50 (2002) 4165–4175.
[40] D.J. Dunstan, A.J. Bushby, Grain size dependence of the strength of metals: the Hall-Petch effect does not scale as the inverse square root of grain size, Int. J. Plast. 53 (2014) 56–65.
[41] J.C. Slater, Atomic radii in crystals, J. Chem. Phys. 41 (1964) 3199.
[42] J. Friedel, Dislocations in Crystals, Pergamon Press, 1967.
[43] S.P. Joshi, K.T. Ramesh, B.Q. Han, E.J. Lavernia, Modeling the constitutive response of bimodal metals, Met. Trans. A 37A (2006) 2397–2404.
[44] H. Yoshinaga, S. Matsuo, H. Kurishita, Dislocation density and internal stress in an Al-5.7 at% Mg alloy, Trans. Jpn. Inst. Met. 26 (6) (1985) 423–432.
[45] R.E. Smallman, R.J. Bishop, Modern Physical Metallurgy and Materials Engineering, Butterworth-Heinemann, 1999.
[46] T.W. Clyne, P.J. Withers, An Introduction to Metal Matrix Composites, Cambridge University Press, 1995.